Electronic Supplementary Information

Modulating Microenvironment of AuPd Nanoparticles by Metal-Organic Frameworks for Selective Methane Oxidation

Jianfei Sui,‡[a] Ming-Liang Gao,‡[a] Chengyuan Liu,[b] Yang Pan,[b] Zheng Meng,*[a] Daqiang Yuan,[c] and Hai-Long Jiang*[a]

[a]Department of Chemistry, University of Science and Technology of China, Hefei, Anhui 230026, P.R. China

[b]National Synchrotron Radiation Laboratory (NSRL), University of Science and Technology of China, Hefei, Anhui 230029, P.R. China

[c]State Key Laboratory of Structural Chemistry, Fujian Institute of Research on the Structure of Matter, Chinese Academy of Sciences, Fuzhou 350002, P. R. China

*E-mails: zhengmeng@ustc.edu.cn (Z. M.) jianglab@ustc.edu.cn (H.-L. J)

‡These authors contributed equally to this work.

S1. Materials and Instruments

All chemicals were purchased from commercial sources and were used without further treatment unless otherwise stated: zirconium tetrachloride ($ZrCl_4$, Aladdin Industrial Corporation, 98%), copper chloride ($CuCl_2 \cdot 2H_2O$, Sinopharm Chemical Reagent Co., Ltd.), N,N-dimethylformamide (DMF, Sinopharm Chemical Reagent Co., Ltd., AR), methanol (MeOH, Sinopharm Chemical Reagent Co., Ltd., AR), glacial acetic acid (AcOH, Sinopharm Chemical Reagent Co., Ltd., AR), acetone (Sinopharm Chemical Reagent Co., Ltd., AR), 30% hydrogen peroxide (H_2O_2, Sinopharm Chemical Reagent Co., Ltd., AR), terephthalic acid (H_2BDC, TCI, >99%), deuterium oxide (D, 99.9%, Adamas-beta®), chloroauric acid hexahydrate ($H_2AuCl_4 \cdot 4H_2O$, Shaanxi Kaida Chemical Engineering Co., Ltd.), and potassium chloropalladite (K_2PdCl_6, Shaanxi Kaida Chemical Engineering Co., Ltd.).

Deionized water was obtained by reversed osmosis (a specific resistance of 18.25 MΩ·cm) followed by ion-exchange and filtration (Cleaned Water Treatment Co., Ltd., Hefei). Powder X-ray diffraction (XRD) patterns were obtained on a Japan Rigaku MiniFlex 600 anode X-ray diffractometer using graphite-monochromated Cu Kα radiation (λ= 1.54178 Å). The contents of Au, Pd, and Cu in the samples were quantified by an Optima 7300 DV inductively coupled plasma atomic emission spectrometer (ICP-AES). Nitrogen sorption measurements were performed by using an automatic volumetric adsorption equipment (Micrometritics ASAP 2020). Field-emission scanning electron microscopy (FE-SEM) was carried out on Zeiss Supra 40 scanning electron microscope at an acceleration voltage of 5 kV with a field emission

scanning electron microanalyzer. The transmission electron microscopy (TEM), high-resolution TEM (HRTEM), and aberration-corrected high-angle annular dark-field scanning transmission electron microscopy (HAADF-STEM) were acquired on field-emission transmission electron microscope (JEOL-2100F) with an electron acceleration energy of 200 kV, respectively. X-ray photoelectron spectroscopy (XPS) measurements were conducted by using an ESCALAB 250 high performance electron spectrometer equipped with monochromatized Al Kα (hν = 1486.7 eV) as the excitation source. Diffuse reflectance infrared Fourier transform (DRIFT) spectra were recorded on a Nicolet™ iS™ 10 FTIR spectrometer equipped with an MCT detector in the 4000 to 400 cm^{-1} range. The Near-Ambient Pressure X-ray Photoelectron Spectroscopy (NAP-XPS) spectra were collected on SPECS NAP-XPS instrument. The CH_4 temperature-programmed desorption combined with mass spectrometric analysis (TPD-MS) was conducted by AutoChem II 2920 Micromeritics instrument. Typically, 50 mg catalyst was loaded into a U-shaped quartz reactor, which was first treated in Ar at 350 °C for 1 h and then cooled down to 50 °C. Next, the sample was heated to 300 °C at a heating rate of 10 °C·min^{-1} in 10% CH_4 in Ar (20 mL·min^{-1}), during which, the outlet of the gas line was connected to a mass spectrometer. The time-resolved CH_4 catalytic oxidation reaction was examined via an *in operando* Synchrotron Radiation Photoionization Mass Spectrometry (SR-PIMS), which was performed on the combustion station of the National Synchrotron Radiation Laboratory (NSRL, Hefei, China). The composition of the liquid sample was analyzed by online SR-PIMS. The sample was crossed and ionized by synchrotron VUV light, and then analyzed by a

homemade time-of-flight mass spectrometer (TOF-MS). The ion signal was amplified with a VT120C preamplifier (EG&G, ORTEC, Oak Ridge, TN) and recorded by a P7888-2 multiscaler (FAST Comtec, Germany).

S2. Experimental Section

Synthesis of UiO-66: The UiO-66 was synthesized following the previous reports with some modifications.[S1, S2] Typically, 40.8 mg $ZrCl_4$ (0.175 mmol), 26.6 mg 1,4-benzenedicarboxylic acid (BDC, 0.16 mmol), 10 mL DMF and 0.5 mL acetic acid were added to a 20 mL glass vial followed by ultrasonic treatment for 5 minutes. The vial was then sealed and placed into a preheated oven at 120 ºC for 24 h. The powder was separated by centrifugation and washed with DMF and acetone. The above-synthesized UiO-66 was immersed in acetone for three days to exchange out DMF and activated at 120 ºC under vacuum for 12 h.

Synthesis of UiO-66$_x$: The UiO-66$_x$ was synthesized following the previous reports with some modifications.[S1, S2] Typically, 48.00 mg $ZrCl_4$ (0.21 mmol) was added to 6 mL DMF and 37.00 mg 1,4-benzenedicarboxylic acid (BDC, 0.206 mmol) was added to 6 mL DMF. Then, these two solutions were mixed together in a glass vial after ultrasonic treatment for 5 minutes. After that, different equivalents of glacial acetic acid (0-2.36 mL, 0-200 mmol) and 10 µL deionized water were added, sealed, and placed into a preheated oven at 120 ºC for 24 h. The powder was separated by centrifugation and washed with DMF and acetone. The above-synthesized UiO-66$_x$ was immersed in acetone for three days to exchange out DMF and activated at 120 ºC under vacuum for 12 h.

Synthesis of Cu-UiO-66$_x$: The Cu-UiO-66$_x$ was synthesized following the previous report with some modifications.[S3] Typically, 100 mg UiO-66$_x$ and 300 mg $CuCl_2 \cdot 2H_2O$ were mixed in 15 mL DMF in a 25 mL microwave vessel by sonication

for 5 minutes. The microwave vessel was sealed and heated to 85 ºC by microwave reactor (CEM Discover SP, 300W), and kept at 85 ºC for 30 min under continuous stirring. The powder was separated by centrifugation and washed with DMF and acetone. The above-synthesized UiO-66_x was immersed in acetone for three days to exchange out DMF and activated at 120 ºC under vacuum for 12 h.

Synthesis of AuPd@UiO-66 and AuPd@Cu-UiO-66_x: Typically, 50.0 mg activated UiO-66 or Cu-UiO-66_x was put in a porcelain crucible and a mixture of a certain amount of 1 mol/mL $HAuCl_4$ and 1 mol/mL K_2PdCl_6 aqueous solution (Au/Pd = 3.5: 1.5 and the total amount of metal is 5 wt%) was added. Then, 200 μL acetone was added into the mixture and stirred with a glass rod at 80 °C to remove the solvent. This procedure was repeated twice and the harvested sample was dried in an 85 °C oven for 1 hour. The obtained powder was treated in a stream of 20% H_2/Ar (40 mL·min^{-1}) at 200 °C for 2 h to yield AuPd@UiO-66 or AuPd@Cu-UiO-66_x.

Catalytic Activity Evaluation

In a typical experiment, the methane oxidation reaction was performed in a 25 mL Teflon-lined type Teflon autoclave (NS25-P5-T3-SS1-SV, Anhui Kemi Instrument Co., Ltd.). The vessel was first charged with 27 mg catalyst, 0.5 mL H_2O_2, and 9.5 mL H_2O. The autoclave was then purged with methane twenty times and pressurized to 30 bar CH_4 (90%, Ar as balance gas). The autoclave was heated to the desired temperature (70 °C) with stirring for 30 min. The reaction mixture was cooled down in an ice-water bath for 30 min before analysis. The gaseous phase products were analyzed by gas chromatography (Shimadzu GC-2014) with a thermal conductivity detector (TCD). The

liquid phase products were confirmed and quantified by ^{1}H-NMR on a 400 MHz Bruker AVANCE III NMR spectrometer. Typically, 400 μL of sample and 200 μL of D_2O (0.01% dimethyl sulfoxide as internal standard) were placed in an NMR tube together. The spectra were recorded using a solvent suppression program in order to minimize the signal arising from the solvent.

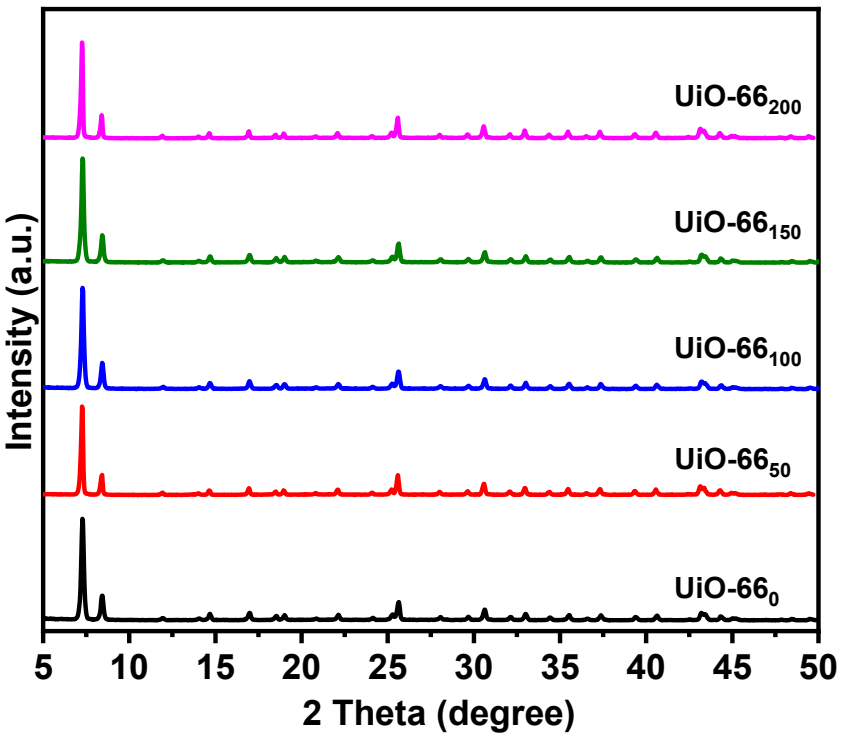

Figure S1. Powder XRD patterns of UiO-66_x (x = 0, 50, 100, 150, 200)

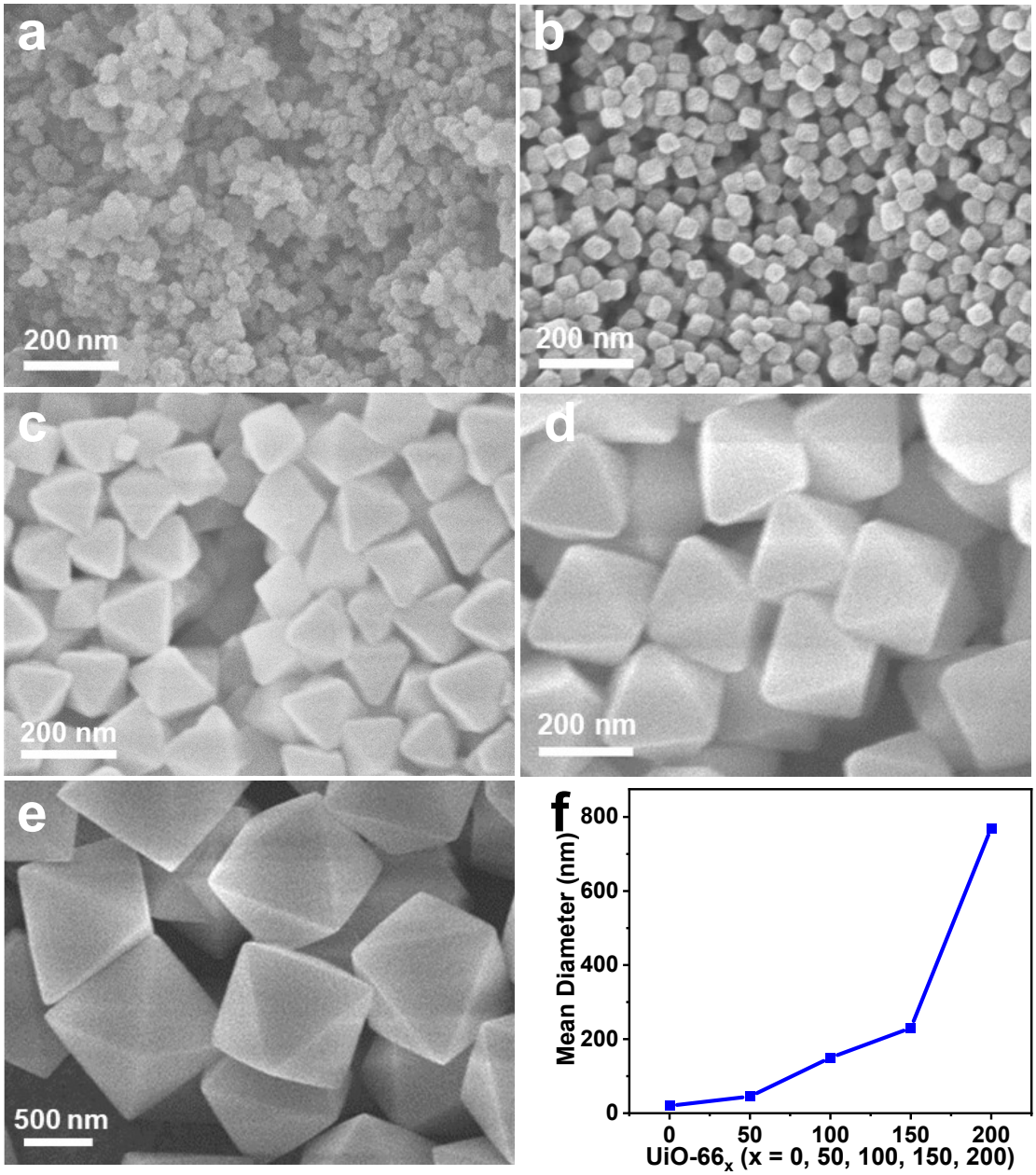

Figure S2. SEM images of a) UiO-66_0, b) UiO-66_{50}, c) UiO-66_{100}, d) UiO-66_{150}, e) UiO-66_{200}; and (f) the mean diameters of MOF particles obtained in (a-e).

The sizes of MOF particles gradually increase and the morphology changes from intergrown prototypes to octahedral nanocrystals, along with more acetic acid involved in the MOF synthesis. In this work, UiO-66 is used to the encapsulate the catalytic active AuPd NPs. Theoret1ically, UiO-66 contains two separate cages, a tetrahedron cage of 7.5 Å, another an octahedron cage of 12 Å, and a pore aperture of 6 Å [S4]. Our

experimental results (Supplementary Fig. 12) also show that pore size distributions of the AuPd@Cu-UiO-66$_x$ are mostly in the range of 7.5-15 Å. All these dimensional values are significantly larger than the kinetic diameter of CH_4, H_2O_2, and CH_3OH, which are respectively 3.8 Å [S5], 2.8 Å [S6], and 3.6 Å [S7]. The kinetic study for the CH_4 adsorption by UiO-66 by Abdullah et al. has shown that, at 3 bar and room temperature, it takes only three minutes for the CH_4 adsorption to get saturated [S8]. At a higher temperature and pressure (70 °C and 30 bar) in our experiment, much faster diffusion is expected. And for H_2O_2 and CH_3OH which have smaller kinetic diameters, faster diffusions are also reasonable. Compared with the time scale of the mass transfer which is likely within just a few minutes, the reaction time of 1 h used in our experiment is long enough to offset any effect of different mass transfer arisen from different crystallite sizes. Actually, after a careful comparison of the experimental results, we found that AuPd@Cu-UiO-66, AuPd@Cu-UiO-66$_0$, AuPd@Cu-UiO-66$_{50}$, and AuPd@Cu-UiO-66$_{100}$ give very similar amount of total oxygenated products despite that their particle size distribution cover more than one order of magnitude scale. This observation suggests that the possible mass transfer effect arisen from different crystallite sizes is negligible to the outcome of catalytic performance which would otherwise give very different amount of total oxygenated products. In above, the observed different catalytic performance is likely due to distinct chemical nature of the catalysts instead of the morphological differences.

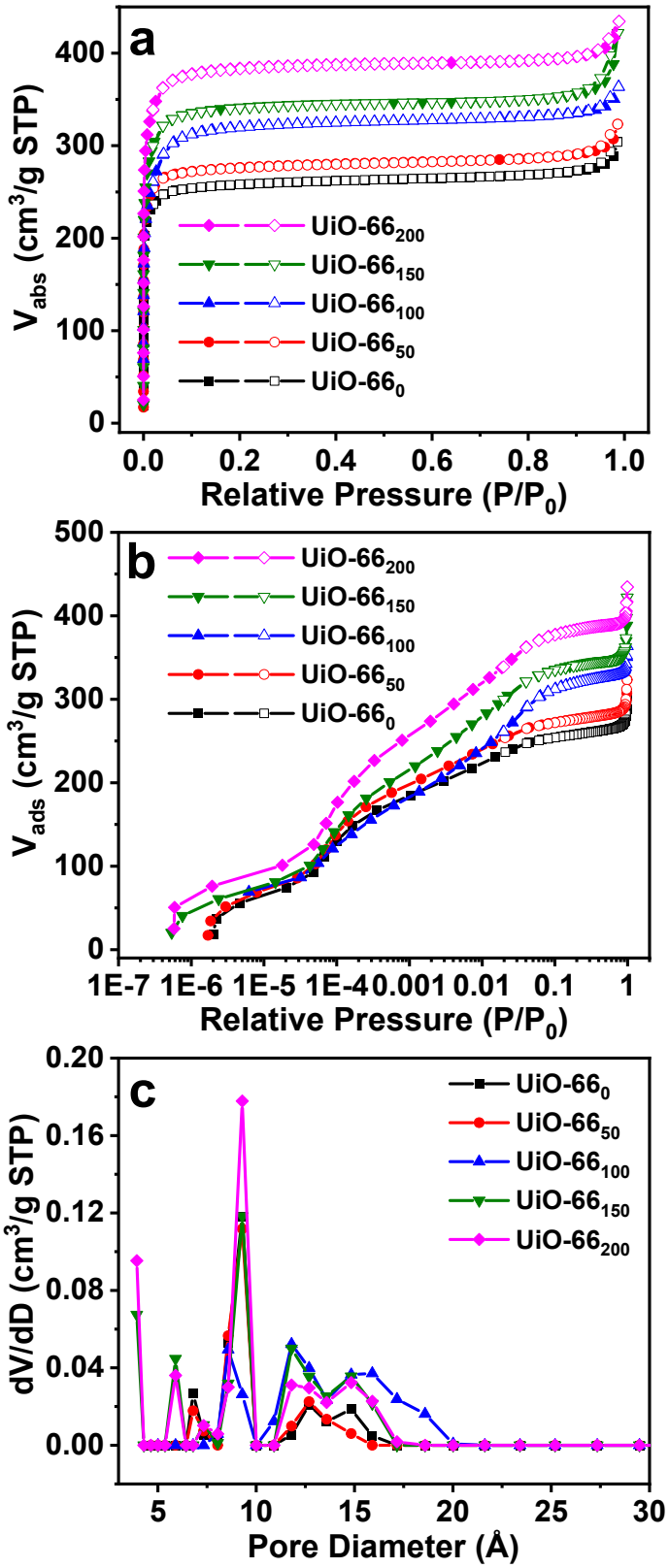

Figure S3. (a) and (b) N_2 sorption isotherms (solid: adsorption curves; open: desorption curves) at 77 K and (c) the corresponding pore size distributions of UiO-66$_x$ (X = 0, 50, 100, 150, 200) based on the density-functional theory (DFT) model.

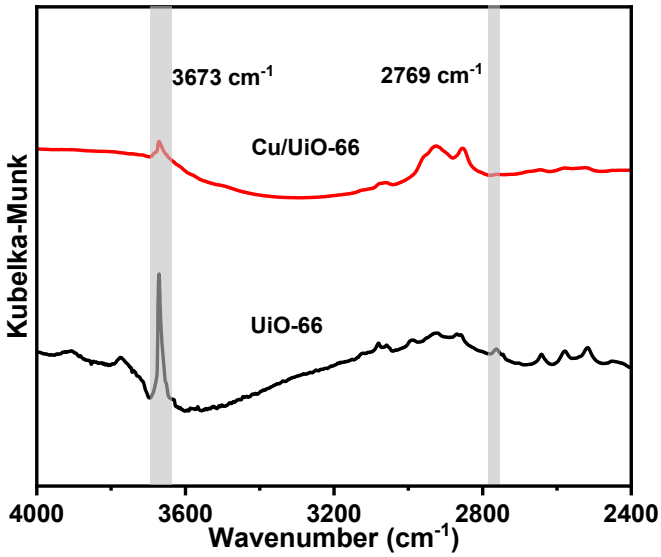

Figure S4. DRIFT spectra of Cu-UiO-66 and UiO-66.

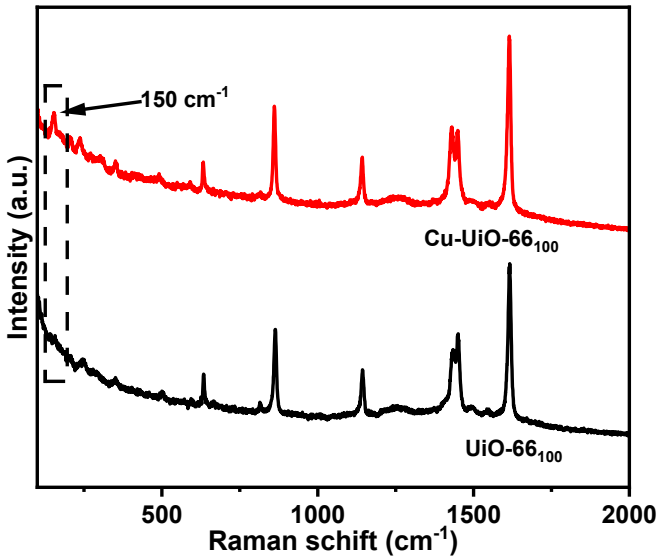

Figure S5. Raman spectra of Cu-UiO-66 and UiO-66.

In this study, the synthesis of UiO-66 with defects and Cu-UiO-66 follows a reported procedure documented by Yaghi and coworkers [S3]. The type of defects produced with the addition of acetic acid modulators has been discussed in a few published articles. It is generally concluded that the missing-linker type defects dominate [S9- S13]. The above diffuse reflectance infrared Fourier transform spectra show that the intensities of peaks at 3673 and 2769 cm^{-1}, respectively attributed to the terminal -OH/-OH_2 and μ_3-OH on the defect sites, are significantly lower in Cu-UiO-66_{200} than those in pristine UiO-66.

This result is consistent with the previous reports that Cu atoms are coordinated to the chelating/linker defect sites of the Zr cluster [S3]. In addition, the Cu-O vibration peak at 150 cm^{-1} has been observed in the Raman spectrum for Cu-UiO-66_{200} (Supplementary Fig. 5), which again validates the analysis of the position of the Cu in Cu-anchored UiO-66 [S14].

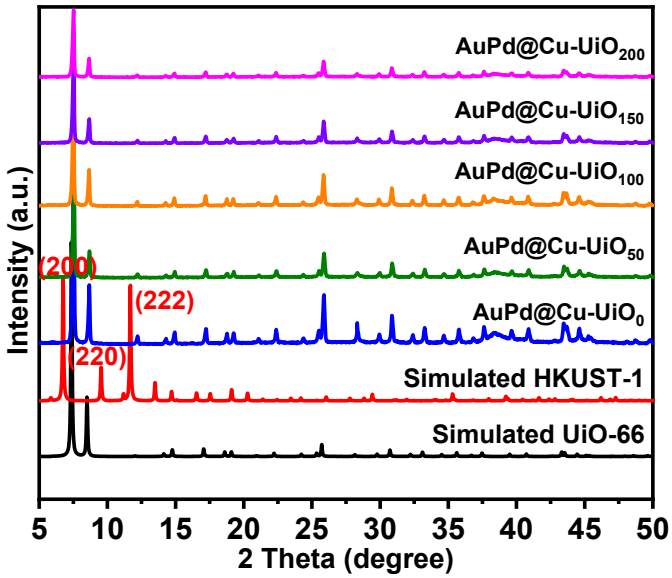

Figure S6. Powder XRD patterns of AuPd@Cu-UiO-66_x (x = 0, 50, 100, 150, 200) samples, simulated UiO-66 and simulated HKUST-1.

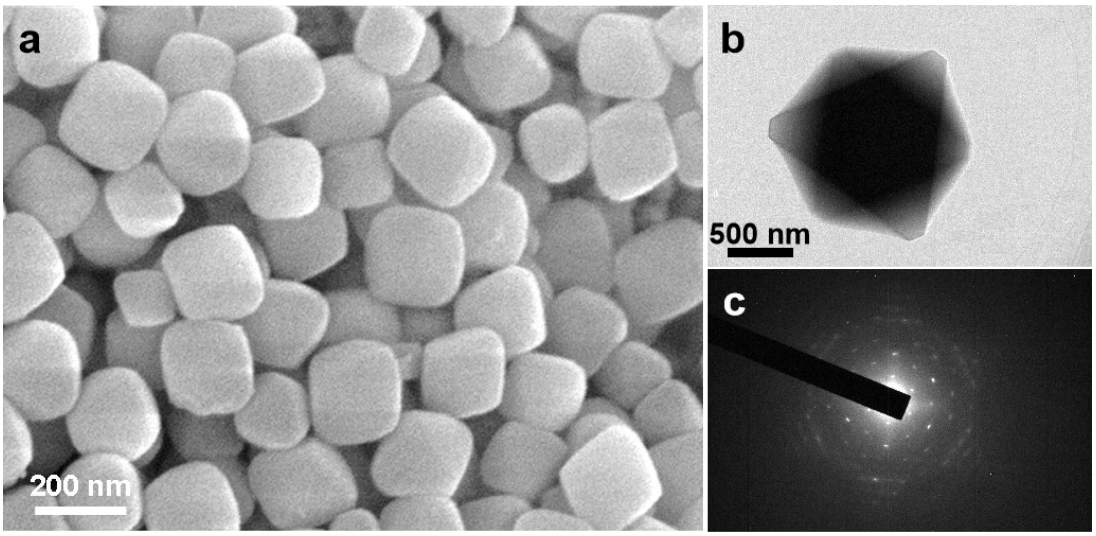

Figure S7. SEM image and selected area electron diffraction (SAED) of TEM of AuPd@Cu-UiO-66_{100}.

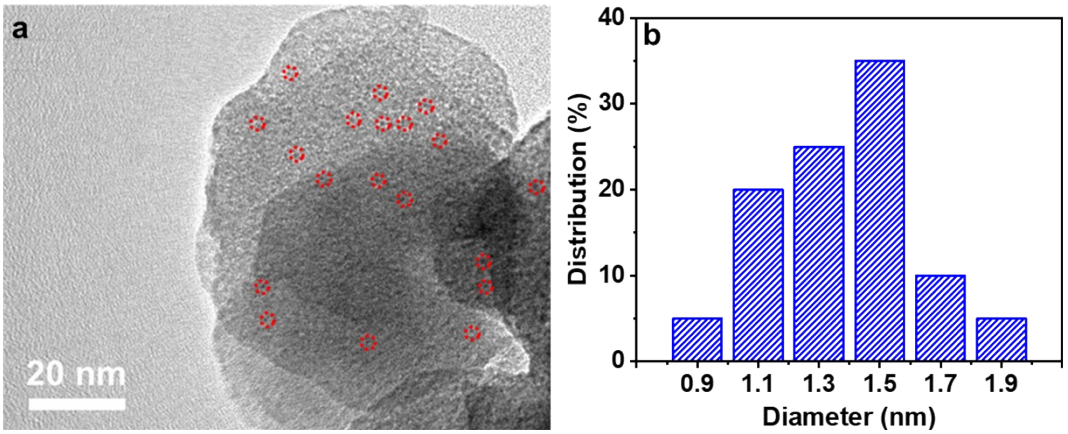

Figure S8. (a) TEM image of AuPd@Cu-UiO-66$_0$ and (b) the corresponding size distribution for AuPd NPs. Some AuPd NPs are highlighted with red circles in (a).

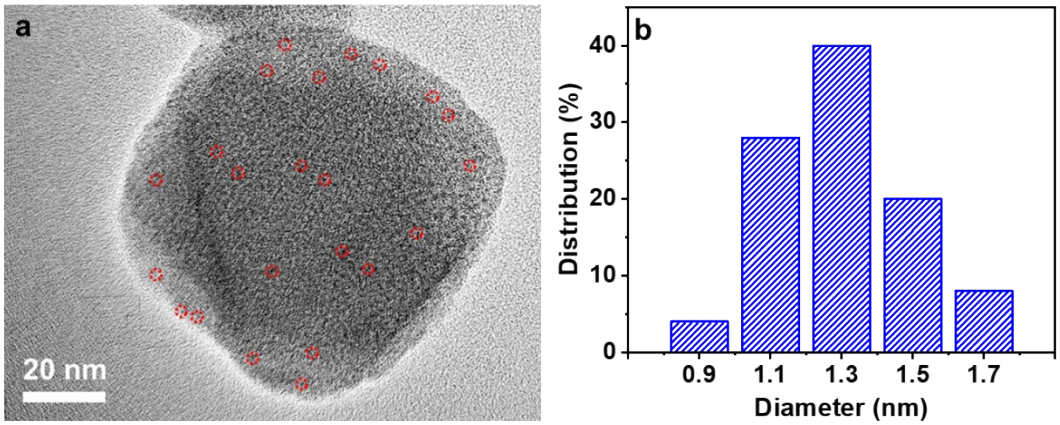

Figure S9. (a) TEM image of AuPd@Cu-UiO-66$_{50}$ and (b) the corresponding size distribution for AuPd NPs. Some AuPd NPs are highlighted with red circles in (a).

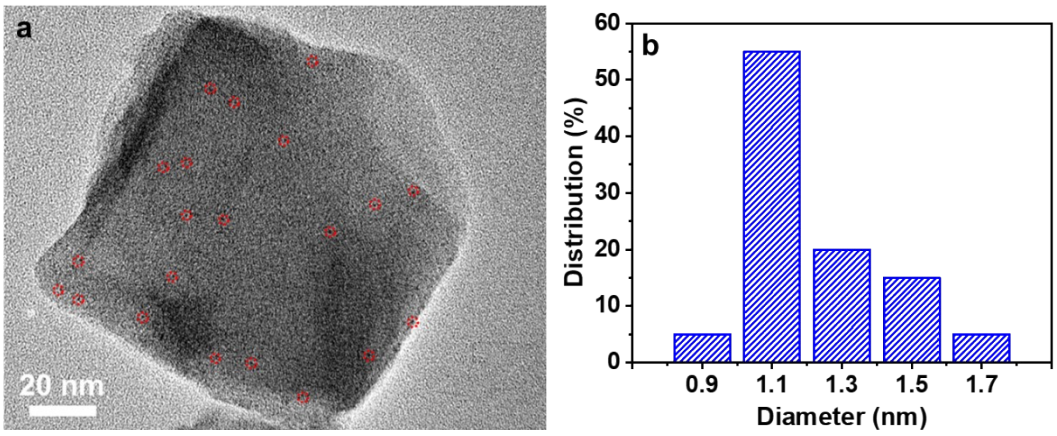

Figure S10. (a) TEM image of AuPd@Cu-UiO-66$_{100}$ and (b) the corresponding size distribution for AuPd NPs. Some AuPd NPs are highlighted with red circles in (a).

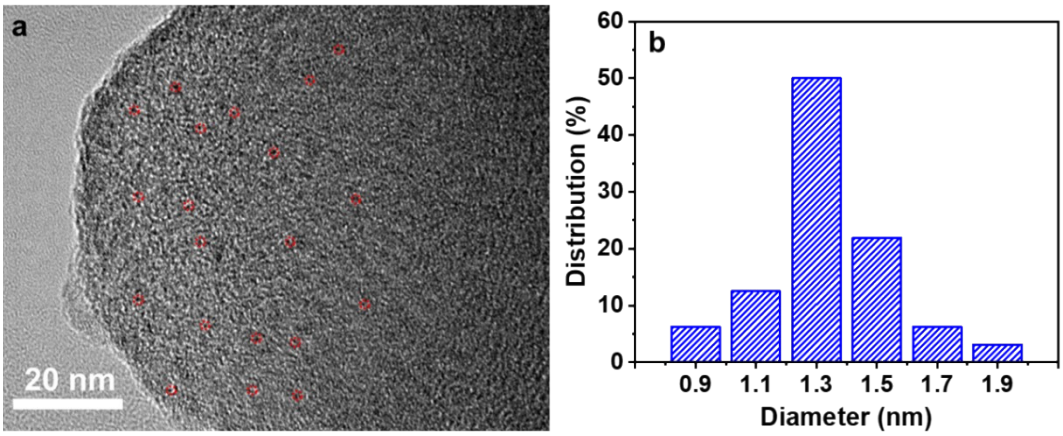

Figure S11. (a) TEM image of AuPd@Cu-UiO-66_{150} and (b) the corresponding size distribution for AuPd NPs. Some AuPd NPs are highlighted with red circles in (a).

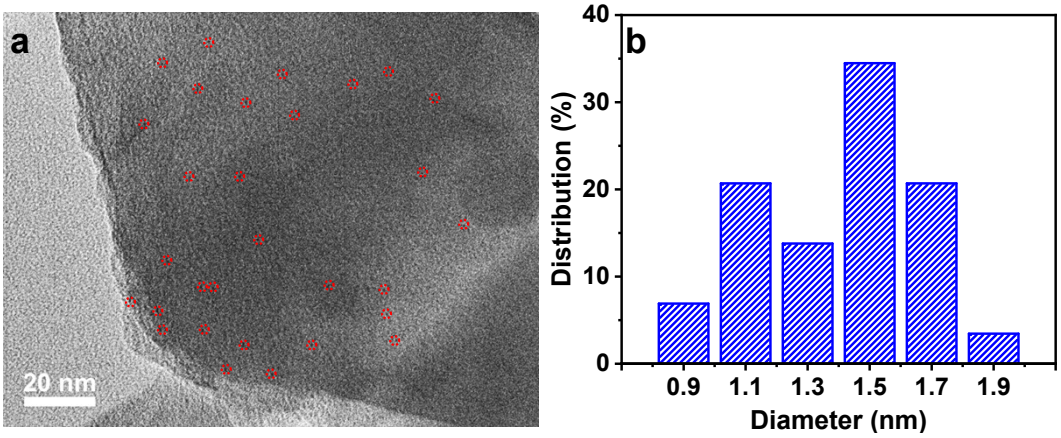

Figure S12. (a) TEM image of AuPd@Cu-UiO-66_{200} and (b) the corresponding size distribution for AuPd NPs. Some AuPd NPs are highlighted with red circles in (a).

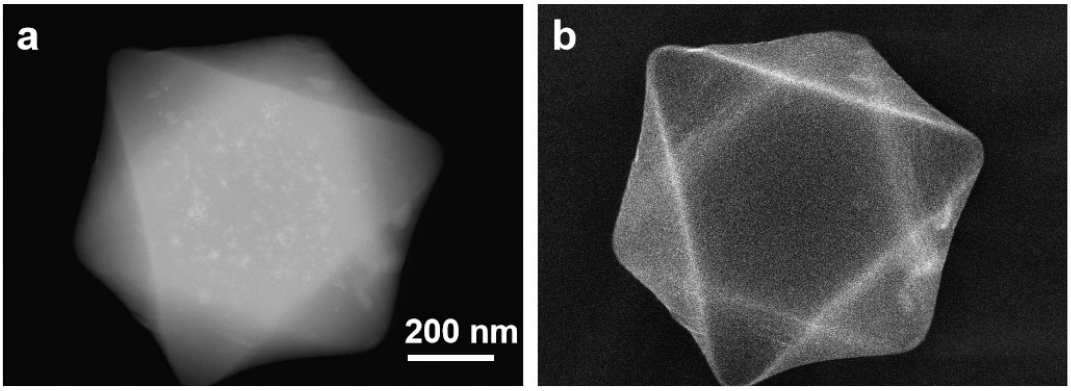

Figure S13. (a) HAADF-STEM and (b) secondary electron STEM (SE-STEM) images of AuPd@Cu-UiO-66_{100}.

The direct comparison between the HAADF-STEM and SE-STEM images acquired at the same location provide direct evidence that the AuPd NPs are located inside the crystallites of AuPd@Cu-UiO-66_{100}.[S15-S17]

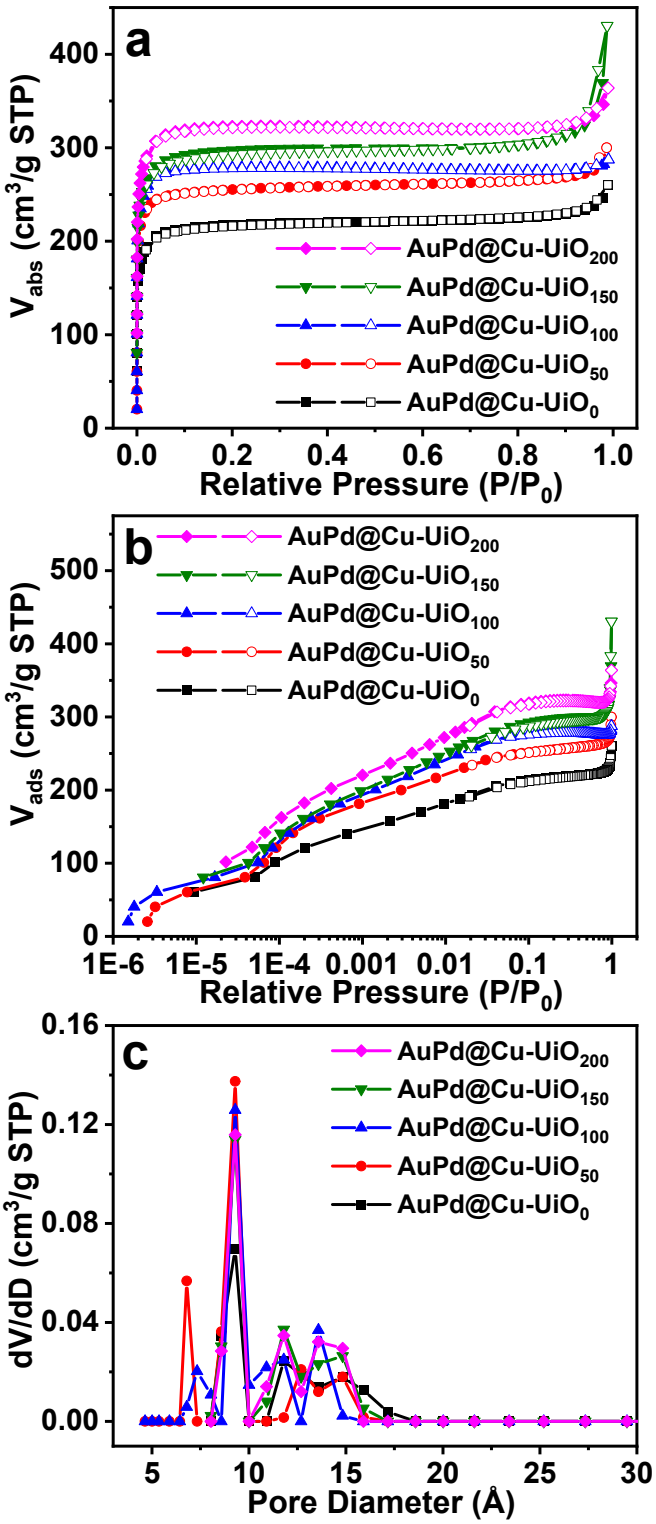

Figure S14. (a) and (b) N_2 sorption isotherms (solid: adsorption curves; open: desorption curves) at 77 K and (c) pore size distributions of AuPd@Cu-UiO-66$_x$ (x = 0, 50, 100, 150, 200) based on the density-functional theory (DFT) analysis.

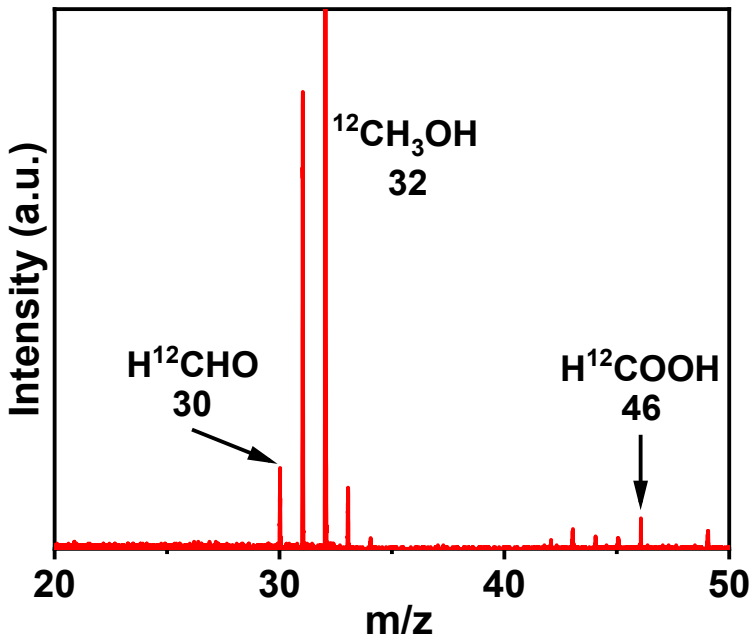

Figure S15. Photoionization mass spectrum of the products using $^{12}CH_3OH$ as reactant.

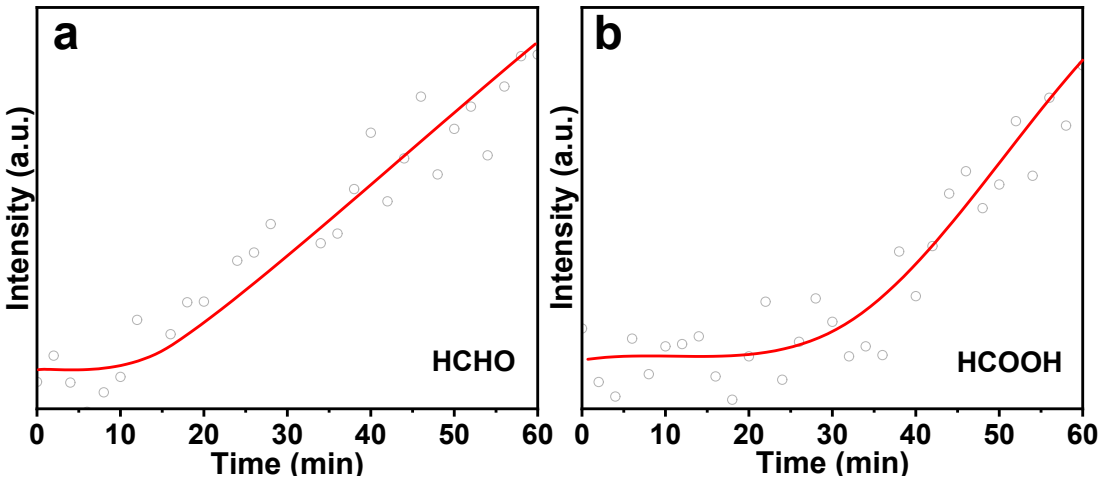

Figure S16. The SR-PIMS data obtained from CH_3OH operando oxidation reaction on AuPd@UiO-66_{100} with H_2O_2 as oxidant at the photon energy of 11.8 eV.

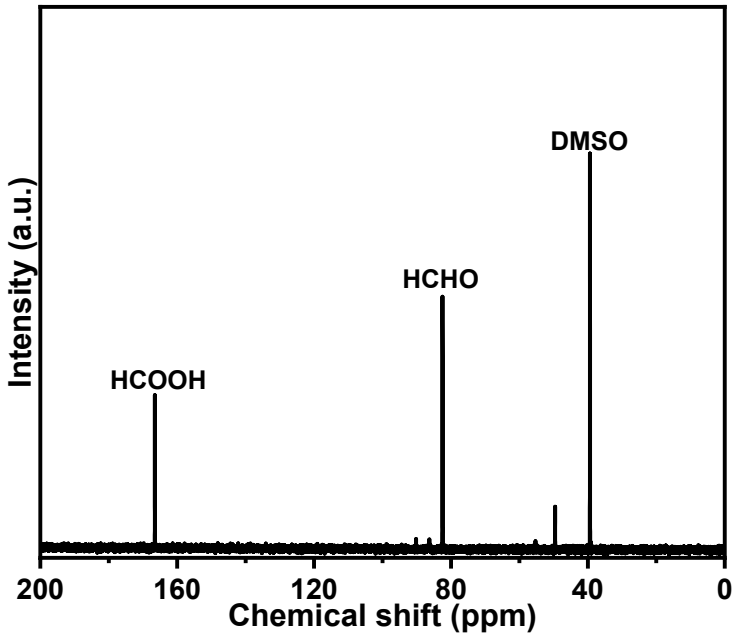

Figure S17. ^{13}C NMR spectra obtained from HCHO oxidation reaction on AuPd@UiO-66_{100} with H_2O_2 as oxidant (DMSO is added to the solvent to be an internal reference).

The chemical shift of HCHO in D_2O is 4.84, which is readily overlapped with the solvent residual signal (chemical shift = 4.79) in ^1H NMR detection. So, the ^{13}C NMR spectrum is adopted in this work.

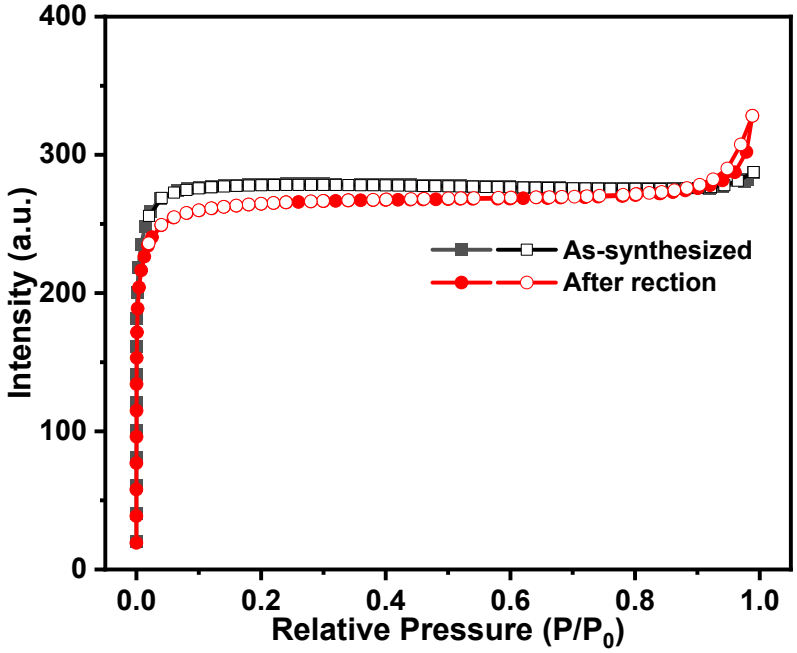

Figure S18. N_2 sorption isotherms (solid: adsorption curves; open: desorption curves)

at 77 K of AuPd@Cu-UiO-66_{100} before and after reaction.

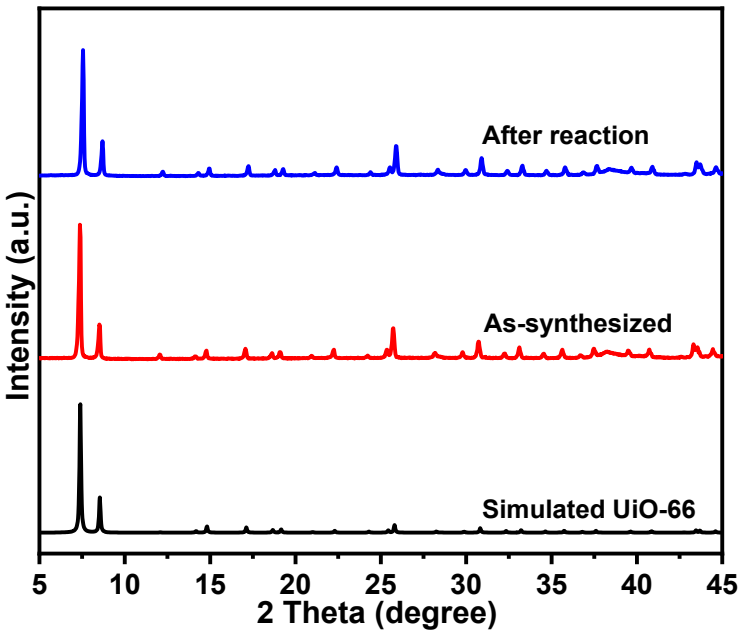

Figure S19. Powder XRD patterns of simulated UiO-66 and AuPd@Cu-UiO-66_{100} before and after reaction.

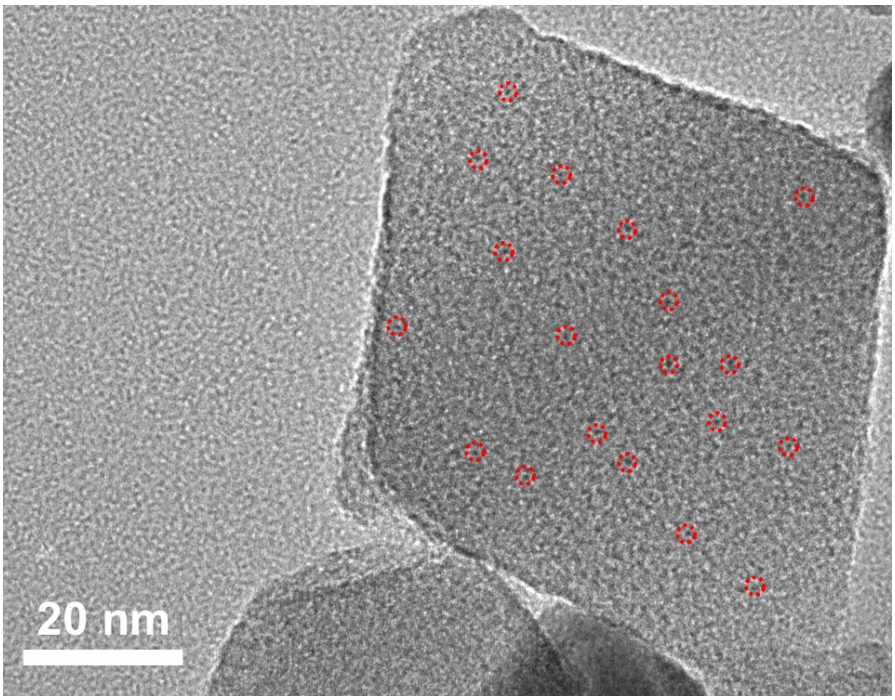

Figure S20. TEM image of AuPd@Cu-UiO-66_{100} after reaction. Some AuPd NPs are highlighted with red circles.

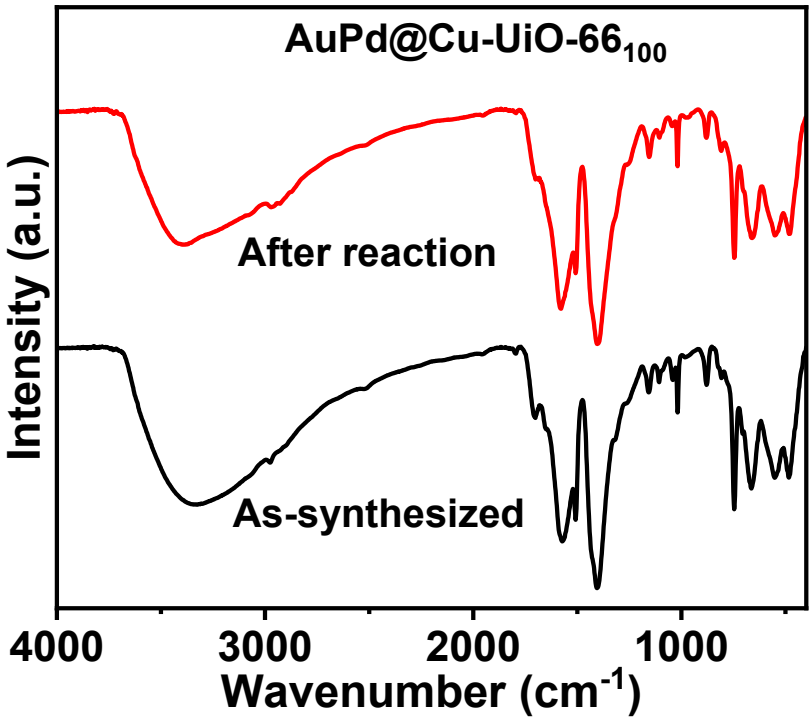

Figure S21. FT-IR spectra of AuPd@Cu-UiO-66_{100} before and after the reaction.

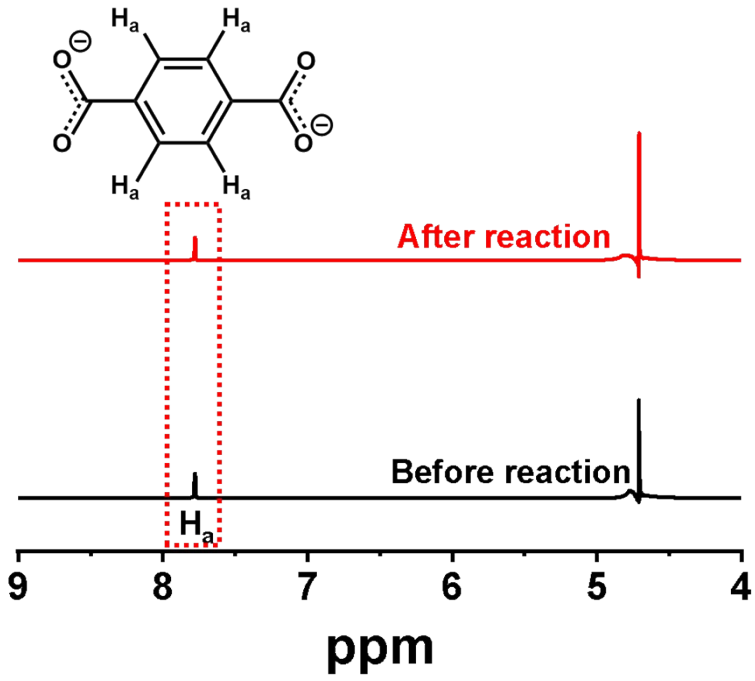

Figure S22. ^{1}H NMR spectra of AuPd@Cu-UiO-66_{100} before and after the reaction.

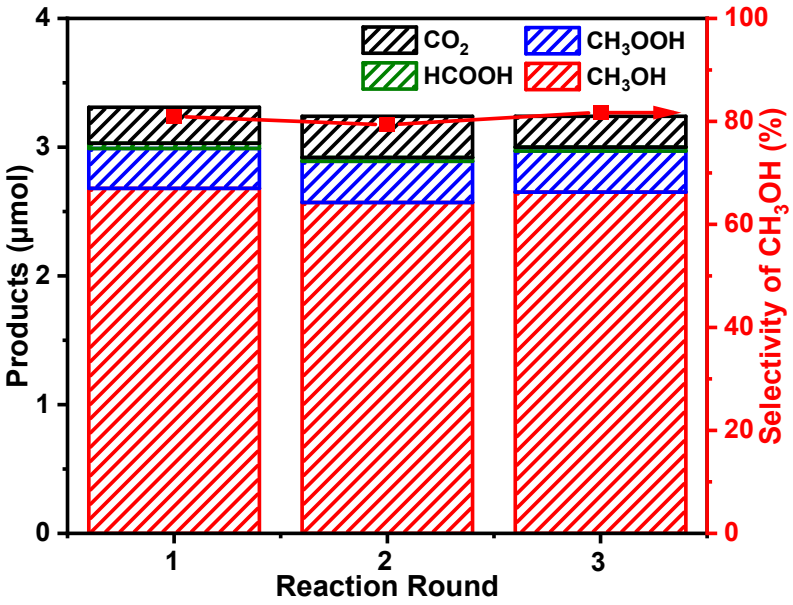

Figure S23. Catalytic recyclability of AuPd@Cu-UiO-66_{100} for the CH_4 oxidation reaction.

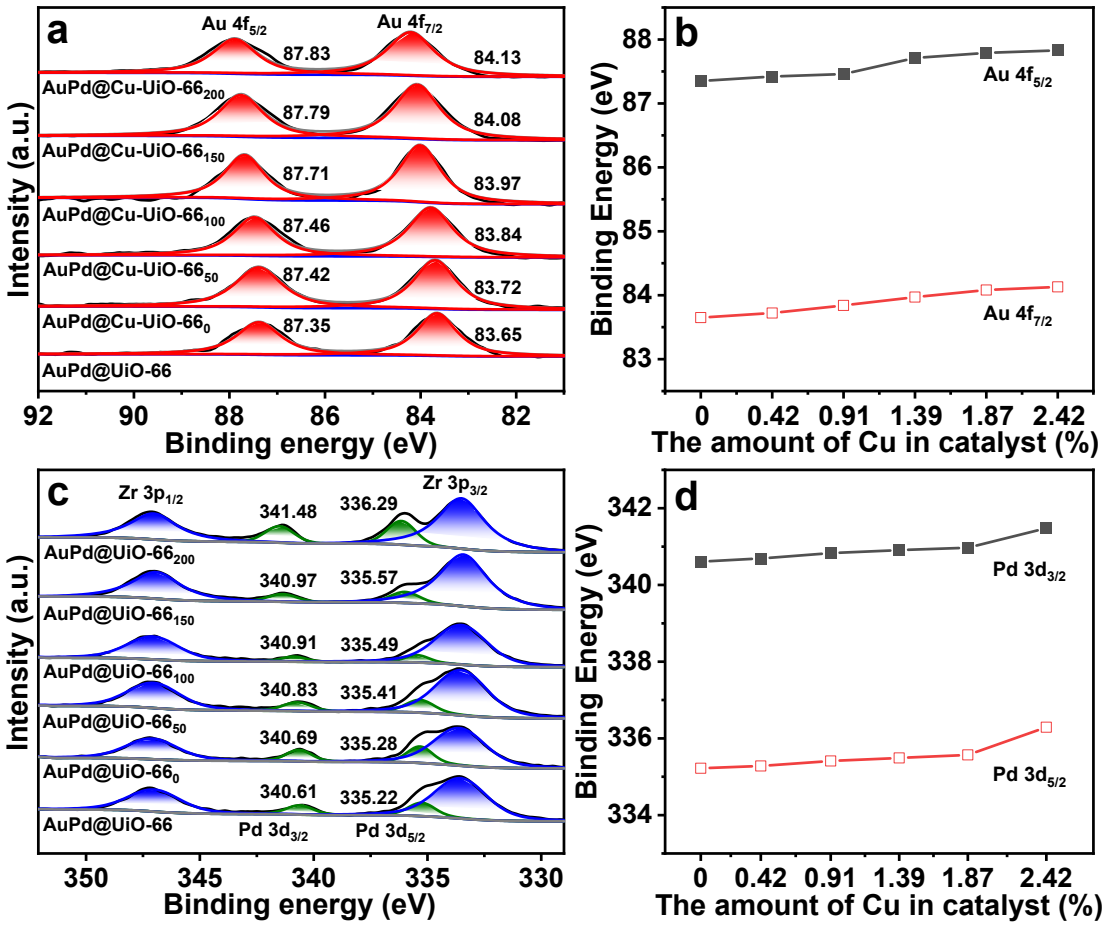

Figure S24. XPS spectra of (a) Au 4f and (c) Pd 3d in AuPd@UiO-66 and AuPd@Cu-UiO-66$_x$ (x = 0, 50, 100, 150, 200). The binding energies of (b) Au 4f and (d) Pd 3d as a function of the Cu amount in the catalyst (the data are from Supplementary Fig. 18a, 18c).

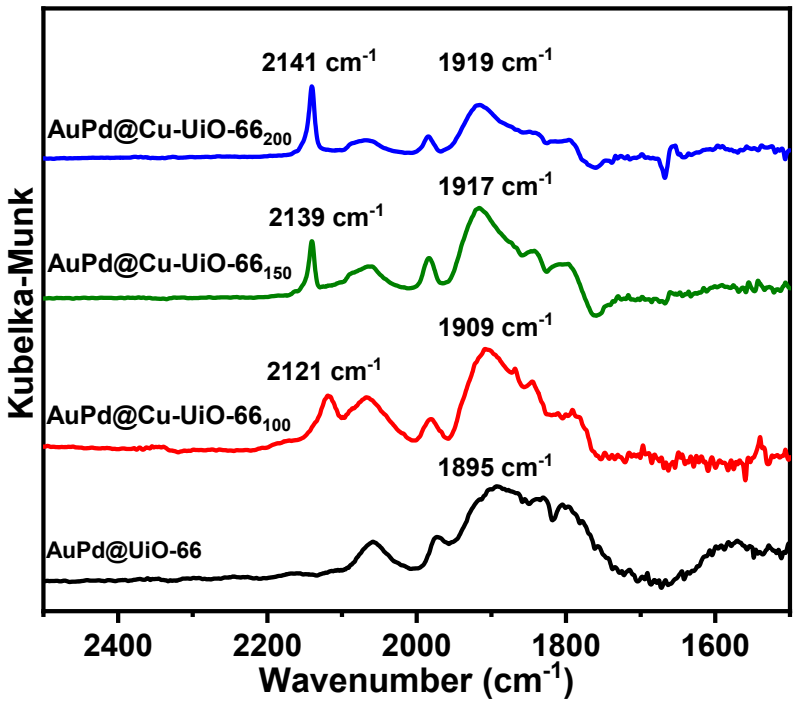

Figure S25. DRIFT spectra of CO adsorbed on AuPd@UiO-66 and AuPd@UiO-66$_x$ (x = 100, 150, 200) after being purged with Ar gas for 30 min.

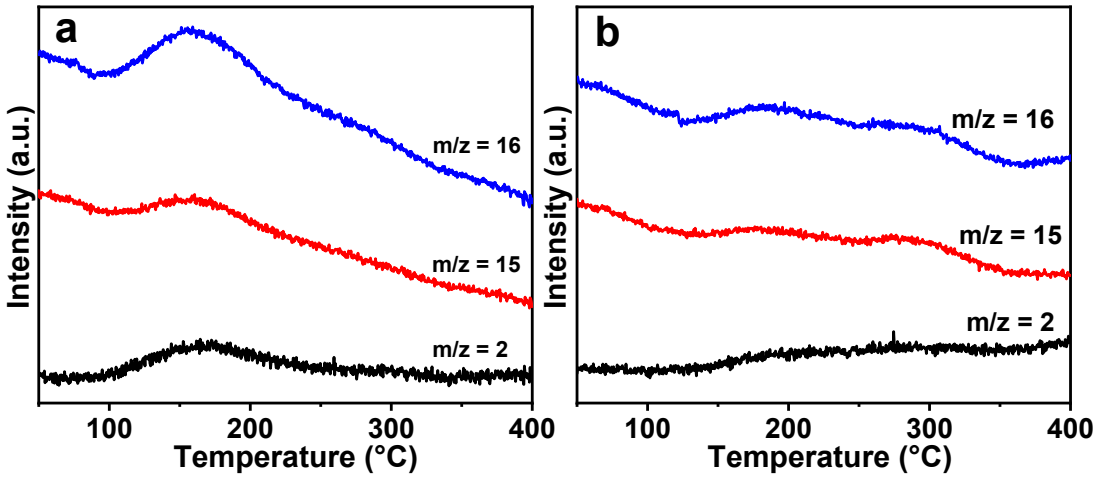

Figure S26. TPD-MS profiles of H_2 (m/z = 2), CH_3 (m/z = 15) and CH_4 (m/z = 16) for (a) AuPd@UiO-66 and (b) AuPd@UiO-66$_{100}$ after adsorbing CH_4 at room temperature. The mass signals of H_2 and •CH_3 are observed with a similar trend, indicating that CH_4 splits to •CH_3 and H_2.

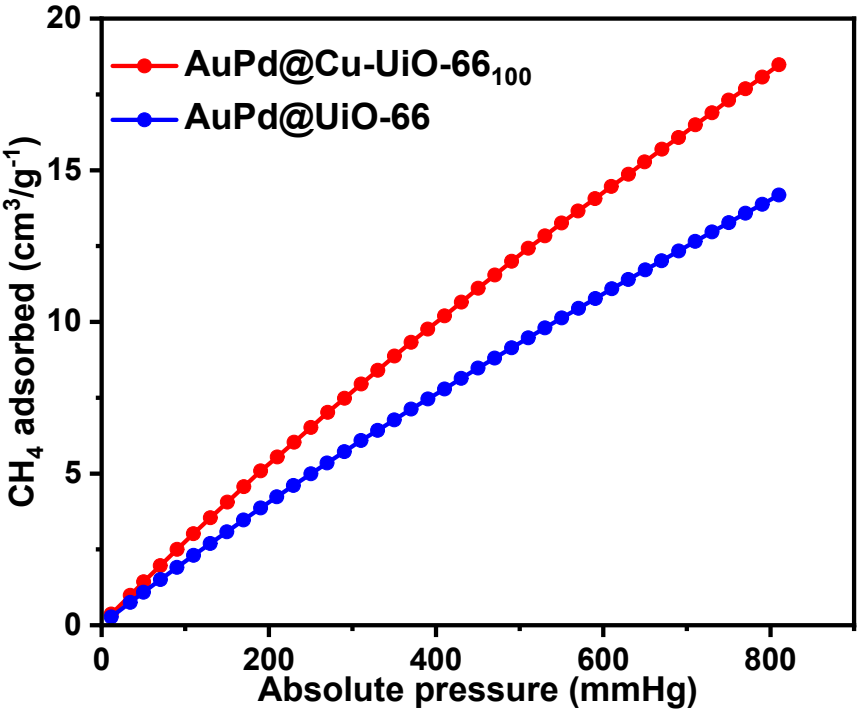

Figure S27. The CH_4 sorption isotherms of AuPd@UiO-66 and AuPd@UiO-66_{100} at 298 K.

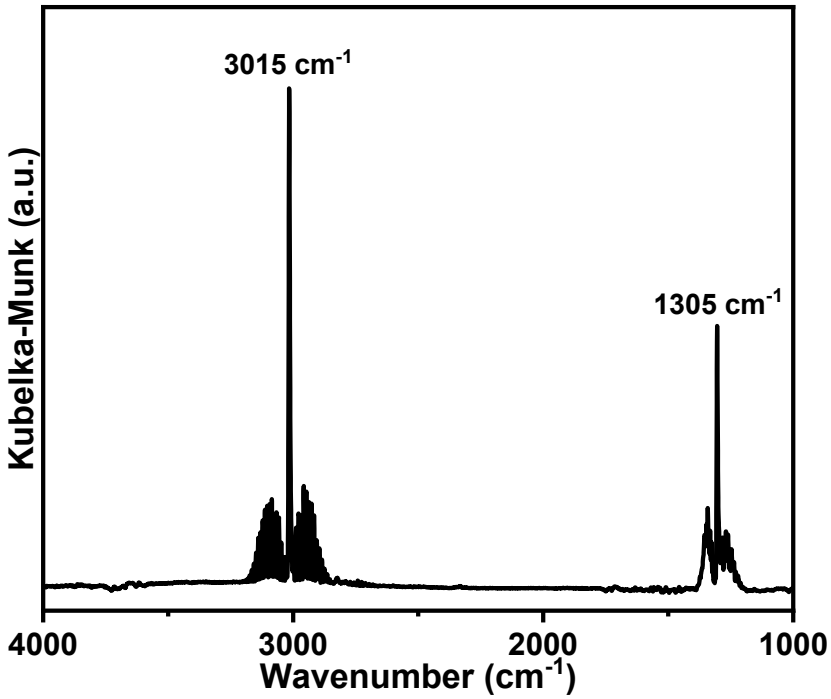

Figure S28. DRIFT spectrum of methane adsorbed AuPd@UiO-66_{100}.

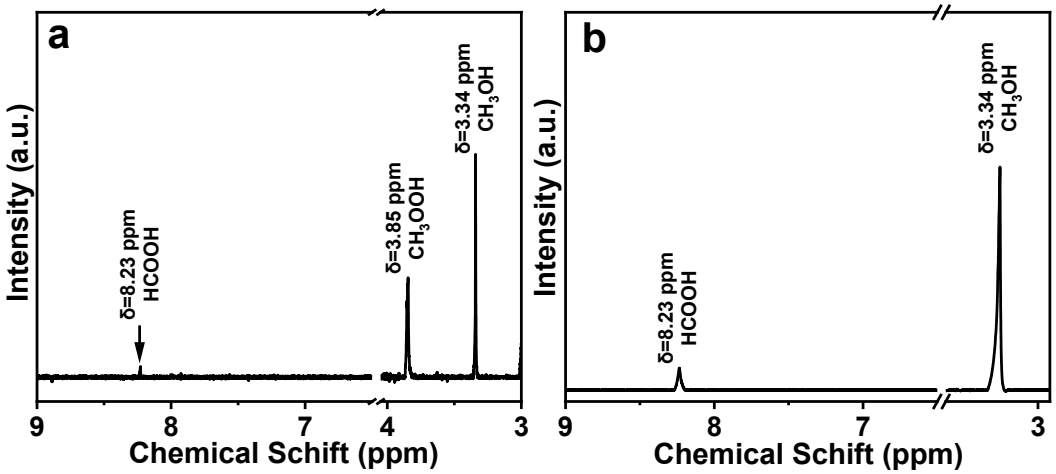

Figure S29. ^{1}H NMR spectra of the reaction products over AuPd@UiO-66$_{100}$ using (a) CH_4 and (b) CH_3OH as the reactant, respectively.

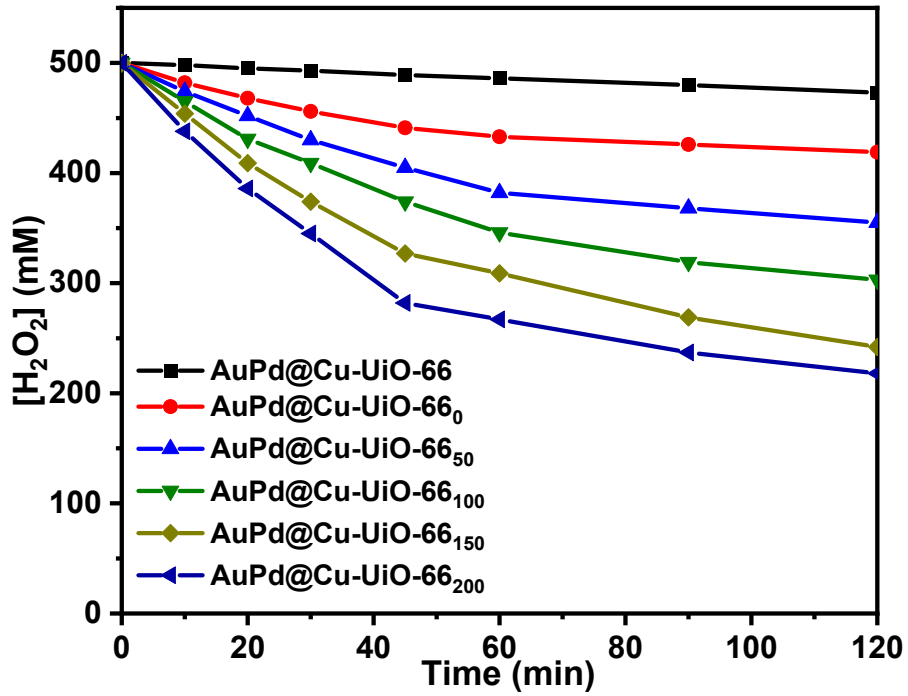

Figure S30. Decomposition of H_2O_2 in H_2O (10 mL) over AuPd@UiO-66 and AuPd@UiO-66$_x$ (x = 0, 50, 100, 150, 200).

Table S1. The Au, Pd, and Cu contents in AuPd@Cu-UiO-66$_x$ (x = 0, 50, 100, 150, 200) based on the ICP-AES results.

Sample	Au content (wt%)	Pd content (wt%)	Cu content (wt%)
AuPd@Cu-UiO-66$_0$	3.41	1.48	0.41
AuPd@Cu-UiO-66$_{50}$	3.52	1.45	0.93
AuPd@Cu-UiO-66$_{100}$	3.51	1.46	1.39
AuPd@Cu-UiO-66$_{150}$	3.44	1.53	1.87
AuPd@Cu-UiO-66$_{200}$	3.47	1.48	2.42

Table S2. Catalytic performance of AuPd@UiO-66, AuPd@Cu-UiO-66$_x$, UiO-66, Cu-UiO-66, Au@UiO-66, Pd@UiO-66, and colloidal AuPd NPs in the CH_4 oxidation.[a]

Entry	Catalyst	C1 organic products ($\mu molg_{cat}^{-1}h^{-1}$)			Total amount	CO_2 ($\mu molg_{cat}^{-1}h^{-1}$)	CH_3OH Sel. (%)	C1 Sel. (%)
		CH_3OH	CH_3OOH	HCOOH				
1	AuPd@UiO-66	119.26	52.59	4.46	176.31	60.74	50.31	74.38
2	AuPd@Cu-UiO-66$_0$	128.15	48.89	3.73	180.77	54.07	54.57	76.97
3	AuPd@Cu-UiO-66$_{50}$	148.89	36.30	3.69	188.88	45.93	63.41	80.44
4	**AuPd@Cu-UiO-66$_{100}$**	**198.52**	**22.96**	**2.96**	**224.44**	**20.74**	**80.97**	**91.54**
5	AuPd@Cu-UiO-66$_{150}$	150.37	20.00	2.23	172.60	23.70	76.60	87.93
6	AuPd@Cu-UiO-66$_{200}$	101.48	17.04	2.22	120.74	18.52	72.87	86.70
7	UiO-66	trace	trace	trace	<2	trace	trace	trace
8	Cu-UiO-66	trace	trace	trace	<2	trace	trace	trace
9	Au@UiO-66	68.89	88.89	4.48	162.26	65.93	30.19	71.11
10	Pd@UiO-66	46.67	17.78	2.24	66.69	20.74	53.38	76.28
11	colloidal AuPd	42.96	119.26	6.62	168.84	17.78	23.02	90.47

[a]Reaction conditions: catalyst 27 mg, CH_4 pressure 30 bar, H_2O_2 0.5 M (aq), 70 °C, reaction time 30 min.

Table S3. Catalytic performance of AuPd@UiO-66_{100} in the CH_4 oxidation.[a]

Entry	H_2O_2	T(°C)	CO_2 (μmol)	CH_3OH (μmol)	CH_3OOH (μmol)	HCOOH (μmol)
1	0	25	trace	trace	trace	trace
2	0.5 M	25	0.11	0.23	0.06	trace

[a]Reaction conditions: catalyst 27 mg, CH_4 pressure 30 bar, reaction time 30 min.

Table S4. Comparison of the elemental contents of AuPd@Cu-UiO-66_{100} before and after the reaction. The metal contents are analyzed by ICP-AES.

Entry	Catalyst	C (%)	H (%)	Au (%)	Pd (%)	Cu (%)
1	AuPd@Cu-UiO-66_{100} before reaction	20.91	2.53	3.51	1.46	1.39
2	AuPd@Cu-UiO-66_{100} after reaction	20.74	2.54	3.48	1.44	1.35

References

[S1] Ma, X.; Wang, L.; Zhang, Q.; Jiang, H.-L. *Angew. Chem. Int. Ed*. **2019**, *58*, 12175-12179.

[S2] Shearer, G. C.; Chavan, S. Bordiga, S.; Svelle, S.; Olsbye, U.; Lillerud, K. P.; *Chem. Mater*. **2016**, *28*, 3749-3761.

[S3] Abdel-Mageed, A. M.; Rungtaweevoranit, B.; Parlinska-Wojtan, M.; Pei, X.; Yaghi, O. M.; Behm, R. J. *J. Am. Chem. Soc*. **2019**, *141*, 5201-5210.

[S4] Winarta, J.; Shan, B.; McIntyre, S. M.; Ye, L.; Wang, C.; Liu, J.; Mu, B. *Cryst. Growth Des*. **2019**, *20*, 1347-1362.

[S5] Aguilar-Armenta, G.; Patiño-Iglesias, M. E.; Leyva-Ramos, R. *Adsorp. Sci. Technol*. **2016**, *21*, 81-91.

[S6] Bienert, G. P.; Schjoerring, J. K.; Jahn, T. P. *Biochim. Biophys. Acta*. **2006**, *1758*, 994-1003.

[S7] Tang, Y.; Dubbeldam, D.; Tanase, S. *ACS Appl. Mater. Interfaces*. **2019**, *11*, 41383-41393.

[S8] Abdullah, A.; Idris, I.; Shamsudin, I. K.; Kim, J.; Othman, M. R. *AIP Conf. Proc.* **2019**, *2124*, 020058.

[S9]Valenzano, L.; Civalleri, B.; Chavan, S.; Bordiga, S.; Nilsen, M. H.; Jakobsen, S.; Lillerud, K. P.; Lamberti, C. *Chem. Mater.* **2011**, *23*, 1700-1718.

[S10] Wu, H.; Chua, Y. S.; Krungleviciute, V.; Tyagi, M.; Chen, P.; Yildirim, T.; Zhou, W. *J. Am. Chem. Soc.* **2013**, *135*, 10525-10532.

[S11] Trickett, C. A.; Gagnon, K. J.; Lee, S.; Gandara, F.; H. Burgi, B.; Yaghi, O. M. *Angew. Chem. Int. Ed*. **2015**, *54*, 11162-11167.

[S12] Ling, S.; Slater, B. *Chem. Sci*. **2016**, 7, 4706-4712.

[S13] Yang, D.; Ortuno, M. A.; Bernales, V.; Cramer, C. J.; Gagliardi, L.; Gates, B. C.; *J. Am. Chem. Soc.* **2018**, *140*, 3751-3759.

[S14] Deng, Y.; Handoko, A. D.; Du, Y.; Xi, S.; Yeo, B. S. *ACS Catal*. **2016**, *6*, 2473-2481.

[S15] Wang, P.; Wang, B.; Liu, Y.; Li, L.; Zhao, H.; Chen, Y.; Li, J.; Liu, S. (. F.).; Zhao, K. *Angew. Chem., Int. Ed.* **2020**, *59*, 23100-23106.

[S16] Lin, L.; Liu, J.; Liu, X.; Gao, Z.; Rui, N.; Yao, S.; Zhang, F.; Wang, M.; Liu, C.; Han, L.; Yang ,F.; Zhang, S.; Wen, X.-D.; Senanayake, S. D.; Wu, Y.; Li, X.; Rodriguez, J. A. and Ma, D. *Nat. Commun.* **2021**, *12*, 6978.

[S17] Wang, H.; Liu, X.; Yang, W.; Mao, G.; Meng, Z.; Wu, Z.; Jiang, H.-L. *J. Am. Chem. Soc.* **2022**, *144*, 22008-22017.